



Cite this: *J. Mater. Chem. A*, 2025, **13**, 40863

Balancing atomic hydrogen supply and nitrate electroreduction for enhanced ammonia synthesis on Pt-Cu₂O/Cu electrocatalysts

Xiaolong Zhu,^a Rong Chen,^a Jiahao Tao,^b Siyi Liang,^c Kai Zhang^{*b} and Wenzheng Yu^{ID *b}

Electrochemical nitrate reduction to ammonia represents a dual-purpose solution for environmental remediation and sustainable ammonia synthesis, yet faces intrinsic kinetic limitations from inefficient hydrogen adsorption, dominant hydrogen evolution pathways, and undesirable byproduct formation. Addressing these challenges, we engineered Pt-Cu₂O/Cu-R and Pd-Cu₂O/Cu-R electrocatalysts via cation exchange. Comprehensive structural characterization confirmed successful synthesis, with Pt-Cu₂O/Cu-R exhibiting enhanced crystallinity and superior hydrogen adsorption capacity. In 0.1 M NaOH/0.1 M NO₃⁻ electrolyte, Pt-Cu₂O/Cu-R achieved exceptional performance metrics with 86.55% faradaic efficiency and 4.16 mg h⁻¹ cm⁻² ammonia yield at 75 mA cm⁻², significantly surpassing Pd-Cu₂O/Cu-R and unmodified Cu₂O/Cu-R. *In situ* spectroscopic studies revealed the operative mechanism that persistent Cu⁺ species activate nitrogenous intermediates while adjacent platinum sites dissociate water, generating reactive hydrogen for sequential hydrogenation. This activity enhancement originates from platinum's unique ability to optimize the kinetic equilibrium between hydrogen generation and nitrate reduction demands. Furthermore, the catalyst retained outstanding operational stability through 20 consecutive electrolysis cycles, demonstrating negligible performance decay. Our work establishes Pt-Cu₂O/Cu-R as an efficient and robust platform for sustainable electrochemical ammonia synthesis.

Received 22nd August 2025
Accepted 21st October 2025

DOI: 10.1039/d5ta06839h
rsc.li/materials-a

Introduction

The imperative to decarbonize ammonia (NH₃) synthesis, a cornerstone of global agriculture and emerging energy systems, is underscored by the energy- and carbon-intensive Haber–Bosch process, which consumes ~2% of worldwide energy expenditure while relying on fossil-derived H₂. The electrochemical nitrate reduction reaction (NO₃RR) presents a transformative alternative, enabling sustainable NH₃ production while remediating pervasive nitrate (NO₃⁻) pollution from industrial effluents and surface waters.^{1,2} The ubiquitous presence of NO₃⁻ in industrial wastewater and surface water bodies positions the electrochemical NO₃RR as a dual-action strategy, enabling concurrent nitrate pollution remediation and nitrogen resource recovery. This environmental burden directly drives ecologically catastrophic eutrophication,

carcinogen-contaminated groundwater systems, and methemoglobinemia risks in vulnerable populations.³ Conventional denitrification technologies, including biological treatment and thermal catalysis, are limited by kinetic constraints, secondary waste generation, and energy-intensive operating conditions. Consequently, efficient electrochemical conversion of waste NO₃⁻ into value-added NH₃ emerges as an essential pathway to close the nitrogen loop, simultaneously mitigating ecological damage and establishing a circular economy for fertilizer production.^{4–6}

Cathode materials critically determine the efficiency of the electrochemical NO₃RR to NH₃, a complex multi-electron/proton transfer process involving eight electrons and nine protons.⁹ Extensive research has focused on transition metal catalysts, particularly Cu, Ni, Co, Fe and Sn, due to their tunable d-band electronic structures and variable nitrate adsorption energetics.^{7–11} Copper-based electrocatalysts occupy a prominent position in this landscape, offering an optimal balance between cost efficiency and intrinsic ability to stabilize key reaction intermediates (*NO₃ and *NO₂) through favorable orbital hybridization.^{12–14} Nevertheless, monometallic Cu systems exhibit intrinsic limitations. Their weak hydrogen binding energy impedes *H coverage during sequential deoxygenation steps, while unoptimized d-band centers lead to suboptimal N-containing intermediate adsorption, resulting in

^aKey Lab of Environmental Engineering, Shaanxi Province, Xi'an University of Architecture and Technology, No. 13 Yanta Road, Xi'an 710055, PR China

^bKey Laboratory of Environmental Aquatic Chemistry, State Key Laboratory of Regional Environment and Sustainability, Research Center for Eco-Environmental Sciences, Chinese Academy of Sciences, Beijing 100085, China. E-mail: kaizhang@rcees.ac.cn; wzyu@rcees.ac.cn

^cMCC Capital Engineering and Research Incorporation Ltd, 7 Jian'an Street, Beijing Economical and Technological Development Area, Beijing 100176, China



the low faradaic efficiencies for NH_3 production.¹⁵ These challenges have driven the development of supported copper architectures, where nanostructuring on conductive substrates enhances active site density and modifies electronic properties.¹⁸ Such configurations achieve high NH_3 selectivity by facilitating nitrate-to-nitrite conversion kinetics and suppressing N–N coupling side reactions.^{16–19} However, the rate-determining proton-coupled electron transfer steps remain kinetically sluggish at environmental temperatures due to high activation barriers.²⁰

To address this, bifunctional designs incorporating Pd or Pt nanoparticles create catalytically synergistic interfaces.²³ The noble metal components serve as hydrogenation promoters.^{21–24} Their near-zero HBE values enable spontaneous H_2 dissociation and $^*\text{H}$ spillover onto adjacent Cu sites, maintaining optimal surface $^*\text{H}$ coverage ($\theta_{\text{H}} > 0.25$ ML) while dynamically suppressing the hydrogen evolution reaction (HER) through competitive site blocking.^{25–28} Besides, Pd/Cu or Pt/Cu interfaces generate interfacial charge redistribution, lowering the energy barrier for $^*\text{NO}$ dissociation through enhanced back-donation into $\text{NO} \pi^*$ orbitals.^{29,30} This synergistic effect concurrently strengthens adsorption of critical intermediates (NH_2 and NH) via covalent bonding interactions, improving NH_3 faradaic efficiencies.^{31–33} We thus posit that Pd/Pt-Cu catalysts enable balancing of NO_3^- activation and $^*\text{H}$ supply, enhancing NO_3^- -to- NH_3 conversion. Despite demonstrated activity, critical knowledge gaps persist regarding electrode architecture engineering and durability optimization.

To address inherent limitations in hydrogen management, novel Pt- $\text{Cu}_2\text{O}/\text{Cu-R}$ and Pd- $\text{Cu}_2\text{O}/\text{Cu-R}$ electrocatalysts on copper foam were synthesized, specifically engineered for efficient nitrate-to-ammonia conversion. The Pt- $\text{Cu}_2\text{O}/\text{Cu-R}$ variant demonstrated superior performance under identical conditions, achieving maximal NH_3 yield at 75 mA cm^{-2} alongside a faradaic efficiency of 86.55%, substantially exceeding the 75.39% of Pd- $\text{Cu}_2\text{O}/\text{Cu-R}$. This performance divergence was attributed to distinct metal–support interactions. Combined *in situ* characterization confirmed two critical phenomena: persistent stabilization of Cu^+ species during nitrate reduction and optimized configuration of key $^*\text{NO}$ intermediates to facilitate hydrogenation. Mechanistically, Cu^+ sites activated nitrogen-containing intermediates while adjacent Pt sites dissociated H_2O , supplying reactive hydrogen for sequential hydrogenation steps. Spectroscopic studies definitively identified atomic hydrogen species participating directly in nitrate reduction. Crucially, Pt achieved a more optimal kinetic balance between $^*\text{H}$ generation and its utilization within the nitrate reduction cascade than Pd, simultaneously minimizing competitive hydrogen evolution. This mechanistic synergy underpinned the exceptional activity and selectivity of Pt- $\text{Cu}_2\text{O}/\text{Cu-R}$.

Experimental section

Preparation of $\text{Cu}_2\text{O}/\text{Cu}$ -based catalysts

Copper membranes (1 mm thickness) were sectioned into pieces measuring 2 cm × 1.5 cm. To remove surface impurities

and oxides and enhance hydrophilicity, the copper pieces underwent a sequential cleaning protocol involving ultrasonic treatment in acetone, 0.1 M aqueous hydrochloric acid, and anhydrous ethanol for 5 min per step. Subsequently, the cleaned membranes were subjected to electrochemical oxidation in a 2 M NaOH electrolyte at a constant current density of 10 mA cm^{-2} . This process yielded a dense layer of blue copper hydroxide ($\text{Cu}(\text{OH})_2$) nanowires, serving as the precursor material. Two of the $\text{Cu}(\text{OH})_2$ nanowire-coated samples were then functionalized *via* immersion in 5 mM solutions of PdCl_2 and PtCl_2 , respectively, for 12 h. The third sample remained unmodified as a control. All three samples were subsequently annealed under an oxygen atmosphere (heating rate: $2 \text{ }^{\circ}\text{C min}^{-1}$) at $200 \text{ }^{\circ}\text{C}$ for 2 h. After cooling to ambient temperature, the samples underwent electrochemical reduction in 1 M NaOH at a constant current of 30 mA for 12 h. This final step produced the target catalysts: Pt- $\text{Cu}_2\text{O}/\text{Cu-R}$, Pd- $\text{Cu}_2\text{O}/\text{Cu-R}$, and $\text{Cu}_2\text{O}/\text{Cu-R}$.

Characterization

Phase purity and crystallinity were determined by X-ray diffraction (XRD) (Bruker D8 Advance; Cu $\text{K}\alpha$, $\lambda = 1.5418 \text{ \AA}$). Raman spectroscopy (Renishaw inVia Qontor; 532 nm excitation) was used to identify vibrational modes and defect states. Morphology and elemental distribution were mapped *via* field-emission scanning electron microscopy (FE-SEM) (JEOL JSM-7800) coupled with energy-dispersive X-ray spectroscopy (EDS). Surface chemistry and oxidation states were analyzed by X-ray photoelectron spectroscopy (XPS) (Thermo Scientific Escalab 250Xi). The atomic-scale structure and lattice parameters were resolved by high-resolution transmission electron microscopy (HRTEM) (FEI Tecnai G2 F30). The concentrations of copper (Cu) and platinum (Pt) were then quantitatively determined using Inductively Coupled Plasma Mass Spectrometry (ICP-MS, Agilent 7900).

Electrochemical measurements

Electrocatalytic nitrate reduction performance was assessed in a standard three-electrode configuration using a Gamry Interface 1010E workstation. The system employed the synthesized catalyst as the working electrode, a platinum foil counter electrode, and an Ag/AgCl (3 M KCl) reference electrode. All measurements utilized an alkaline electrolyte (0.1 M NaOH + 0.1 M NaNO_3) to optimize nitrate reduction kinetics. Linear sweep voltammetry (LSV) and cyclic voltammetry (CV) were performed at 5 mV s^{-1} to evaluate electrode activity and reaction pathways. Potentials were converted to the reversible hydrogen electrode (RHE) scale using: $E_{\text{RHE}} = E_{\text{Ag/AgCl}} + 0.059 \times \text{pH} + 0.200 \text{ V}$. Electrochemical impedance spectroscopy (EIS) probed interfacial kinetics from 0.01 Hz to 100 kHz with an AC amplitude of 5 mV. During the stability test, 20 cycles of two-hour electrolysis were conducted at 75 mA cm^{-2} . The electrolyte was collected after each two-hour electrolysis for product analysis, and fresh electrolyte was used for the next cycle. The NH_3 faradaic efficiency was calculated according to the following equation: $\text{FE}_{\text{NH}_3} = N_{\text{NH}_3} V C_{\text{NH}_3} F / Q$; in this equation, Q



is the total Coulomb count applied, N is the electron transfer number (8 for 1 mol NH_3), V is the cathode chamber's catholyte volume, C_{NH_3} is the NH_3 concentration, and F is the Faraday constant (96 485 C mol $^{-1}$).

Electron paramagnetic resonance (EPR) measurements

Electron paramagnetic resonance (EPR) spectroscopy (Bruker EMXplus) was employed to detect hydrogen radicals (^1H) using 5,5-dimethyl-1-pyrroline N-oxide (DMPO) as a spin trap. Following electrocatalytic nitrate reduction (NO_3RR) at -0.2 V vs. RHE for 5 min in 0.1 M NaOH electrolyte with/without 0.1 M NO_3^- , 0.5 mL of catholyte from the cathodic chamber was rapidly mixed with 0.2 mL of 0.2 M DMPO. The mixture was transferred *via* capillary tube, and spectra were acquired at room temperature.

In situ Raman measurements

In situ Raman spectroscopy (LabRAM Odyssey, 633 nm excitation) coupled with a CHI760E electrochemical workstation was used to probe reaction intermediates under operational conditions. Catalysts were deposited on glassy carbon working electrodes (3 mm diameter), with Pt wire and Ag/AgCl as counter and reference electrodes, respectively. Measurements commenced at open-circuit potential (OCP) in 0.1 M KOH + 0.1 M NaNO_3 electrolyte to establish baseline vibrational features. Potentiostatic *in situ* spectra were then acquired from $+0.2$ V to -0.2 V vs. RHE in 0.1 V increments. At each potential, the system equilibrated for 60 s prior to spectral acquisition to stabilize surface species.

In situ FTIR spectrometry measurements

In situ electrochemical Fourier transform infrared (FTIR) spectroscopy measurements were performed using a Nicolet iN10MX FTIR spectrophotometer (Thermo Fisher Scientific) interfaced with an electrochemical workstation. A custom spectroelectrochemical cell (Tianjin Aida Hengsheng Technology Development Co., Ltd) featured a catalyst-modified Au working electrode at its base. The infrared beam path was configured for reflection from the catalyst surface, passing through a CaF_2 window and an ~ 10 μm thin-layer electrolyte (0.1 M NaOH + 0.1 M NaNO_3). Potential-dependent FTIR spectra were collected in a time-resolved mode at 4 cm $^{-1}$ resolution, averaging 64 scans per spectrum. All experiments were conducted under potentiostatic control, with the applied potential stepped systematically to probe potential-dependent interfacial processes.

Determination of aqueous-phase N content

A calibration curve relating ammonia concentration to absorbance was established using standard solutions prepared from ammonium chloride (NH_4Cl , dried at 105 °C for 2 h). Ammonia nitrogen ($\text{NH}_3\text{-N}$) quantification employed an optimized salicylic acid method. Following appropriate dilution of the post-reaction electrolyte, 2 mL aliquots were sequentially mixed with: (1) 2 mL chromogenic reagent (1 M NaOH containing 5%

(w/v) salicylic acid and 5% (w/v) sodium citrate); (2) 1 mL of 0.05 M sodium hypochlorite (NaClO) solution; and (3) 200 μL of 1.0% (w/v) sodium nitroferricyanide solution. The reaction mixture was vortex-mixed and incubated in darkness for 2 h to facilitate indophenol blue formation. Absorbance of the resulting chromogen was measured at 655 nm using a Shimadzu UV-2600 spectrophotometer, with each sample analyzed in triplicate.

Nitrite concentrations (NO_2^- -N) were quantified by interpolation from a standard calibration curve relating concentration to absorbance. The curve was established using sodium nitrite standard solutions following identical pretreatment protocols. The Griess reagent was prepared by dissolving 2 g sulfanilamide, 0.1 g *N*-(1-naphthyl) ethylenediamine dihydrochloride, and 5 mL phosphoric acid (85% v/v) in 25 mL deionized water. For analysis, the 0.1 mL chromogenic agent was added to the 5 mL diluted sample, followed by vortex mixing and incubation for 20 min at 25 ± 1 °C. Absorbance of the resulting azo dye was measured at 540 nm using a Shimadzu UV-2600 spectrophotometer.

Sodium nitrate (NaNO_3) was dried at 105 °C for 2 h to minimize hydration effects. Standard solutions spanning a concentration gradient were prepared to establish a calibration curve relating nitrate concentration (NO_3^- -N) to UV absorbance. For analysis, 5 mL sample aliquots were diluted with deionized water, acidified with 0.1 mL of 6 M HCl (37% w/w), and thoroughly mixed. After 20 min equilibration at 25 °C, absorbance was measured at 220 nm and 275 nm using a Shimadzu UV-2600 spectrophotometer. Nitrite-corrected absorbance (A) was calculated as: $A = A_{220\text{nm}} - 2A_{275\text{nm}}$, where the factor of 2 corrects for background organic interference.

Results and discussion

Synthesis and characterization

These Pt-Cu₂O/Cu-R, Pd-Cu₂O/Cu-R, and Cu₂O/Cu-R materials were synthesized *via* sequential anodization, cation exchange (Cu^{2+} with $\text{Pd}^{2+}/\text{Pt}^{2+}$), calcination, and electroreduction (Fig. 1). XRD analysis confirmed the structural evolution. The as-calcined samples exhibited characteristic CuO (JCPDS #45-0937) and Cu₂O (JCPDS No. 05-0667) diffraction peaks (Fig. S1).³⁴ After electroreduction, the primary CuO diffraction intensity diminished significantly, accompanied by a concurrent enhancement of Cu₂O (JCPDS #05-0667) and metallic Cu peaks (Fig. 2a). Notably, the Cu₂O (111) diffraction peak intensity at 36.4° was highest for Pt-Cu₂O/Cu-R compared to Pd-

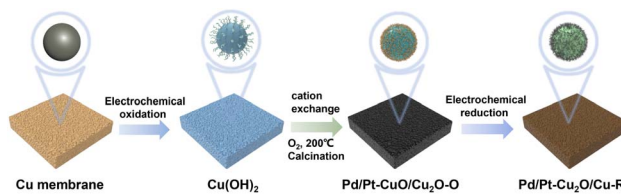


Fig. 1 Schematic illustration of the fabrication process of the Pd/Pt-Cu₂O/Cu-R membrane.



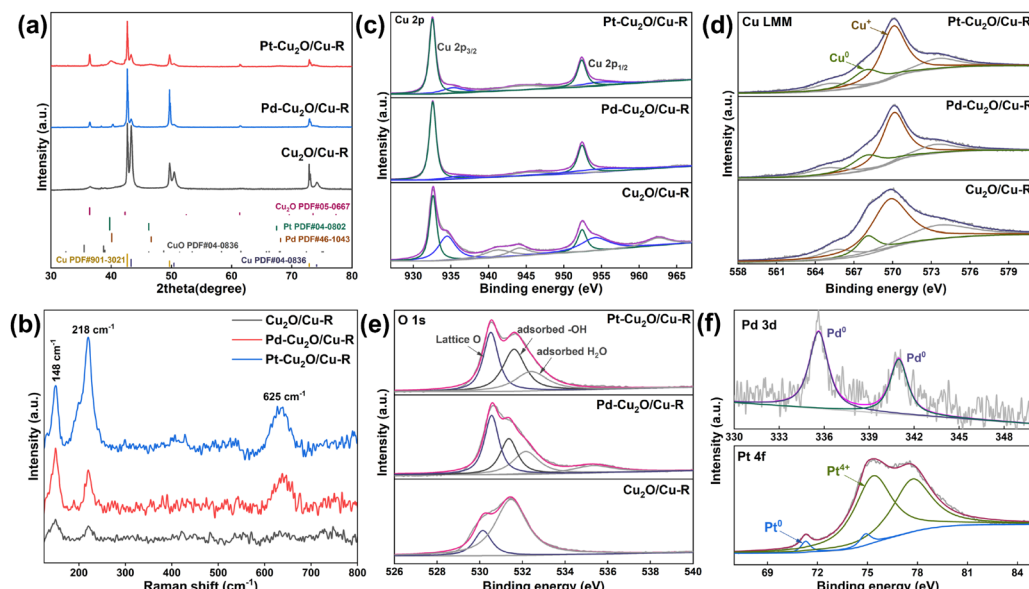


Fig. 2 (a) XRD patterns and (b) Raman spectra of Pt-Cu₂O/Cu-R, Pd-Cu₂O/Cu-R, and Cu₂O/Cu-R; XPS spectra of Pt-Cu₂O/Cu-R, Pd-Cu₂O/Cu-R, and Cu₂O/Cu-R: (c) Cu 2p; (d) AES spectra of Cu LMM; (e) O 1s and (f) Pd 3d and Pt 4f.

Cu₂O/Cu-R and Cu₂O/Cu-R. Furthermore, distinct diffraction peaks corresponding to the Pt (111) and Pd (111) planes were evident in Pt-Cu₂O/Cu-R and Pd-Cu₂O/Cu-R samples, respectively (Fig. 2a).³⁵ Raman spectra of the Cu oxide-based electrodes are presented in Fig. S2 and 2b. CuO and Cu₂O exhibited distinct Cu–O vibrational modes. Characteristic Raman peaks for CuO were observed at 294 cm⁻¹, 347 cm⁻¹, and 635 cm⁻¹.¹² After electroreduction, the spectrum revealed features attributable to Cu₂O: an IR-active peak at 148 cm⁻¹, a second-order overtone at 218 cm⁻¹, and a Cu–O stretching vibration at 625 cm⁻¹. No characteristic Raman peaks were observed for Pd or Pt within the analyzed spectral range.³⁶

X-ray photoelectron spectroscopy (XPS) analysis elucidated the valence states of the catalytic electrodes. Deconvolution of Cu 2p core levels (Fig. S3a) revealed peaks at 932.8 eV (2p_{3/2}) and 952.6 eV (2p_{1/2}) characteristic of Cu⁺/Cu⁰, alongside Cu²⁺ signatures at 934.8 eV and 954.7 eV. The prominent Cu LMM peak observed in Fig. S3b corresponded to the main Cu²⁺ species. Post-electroreduction spectra exhibited dominant Cu⁺/Cu⁰ peaks at 932.6 eV and 952.4 eV, with a residual Cu²⁺ feature attributable to surface oxidation (Fig. 2c).³⁷ Complementary X-ray-induced Auger electron spectroscopy (AES) resolved this ambiguity. The prominent Cu LMM peak at 570.1 eV confirmed Cu₂O, while a weaker feature at 568.1 eV corresponded to Cu⁰ (Fig. 2d).³⁸ Deconvoluted O 1s spectra (Fig. S4 and 2e) showed lattice oxygen (530.6 eV), adsorbed -OH (531.5 eV), and adsorbed H₂O (532.4 eV). Noble metal states were unequivocally assigned. Pt-CuO/Cu₂O-O exhibited Pt 4f peaks at 77.3 eV and 79.6 eV (Fig. S5). Deconvolution of Pt 4f spectra in Pt-Cu₂O/Cu-R revealed two spin-orbit doublets, indicating that Pt⁴⁺ at 75.4 eV and 77.8 eV dominated with minimal Pt⁰ contribution, consistent with surface oxidation during air exposure (Fig. 2f).³⁹ Partial oxidation of Pt species suggested electronic metal–support interactions with Cu₂O. As shown in Fig. S4, Pd-CuO/Cu₂O-O

demonstrated Pd²⁺ peaks at 337.1 eV and 342.9 eV. Pd-Cu₂O/Cu-R showed Pd 3d_{5/2} and 3d_{3/2} peaks. Besides, Pd-Cu₂O/Cu-R exhibited binding energies at 336.3 eV and 341.5 eV, confirming Pd⁰ dominance (Fig. 2f).⁴⁰

Scanning electron microscopy (SEM) imaging revealed Cu₂O nanorods composed of micrometre-long nanowires (Fig. 3a). Sequential treatments generated a Pd-Cu₂O/Cu-R composite, with Pd nanospheres decorating the Cu₂O nanorod surfaces (Fig. 3b). Conversely, Pt deposition preserved the pristine Cu₂O nanorod morphology (Fig. 3c). The SEM images of CuO/Cu₂O-O, Pd-CuO/Cu₂O-O, Pt-CuO/Cu₂O-O are also clearly demonstrated in Fig. S6–S8. Energy-Dispersive X-ray (EDX) spectroscopy elemental mapping confirmed the homogeneous distribution of Cu and O within the Cu₂O/Cu-R composite (Fig. 3d). After Pd deposition, EDX mapping revealed uniform distributions of Cu, O, and Pd throughout the Pd-Cu₂O/Cu-R sample (Fig. 3e). A similarly homogeneous distribution of Cu, O, and Pt was observed for Pt-Cu₂O/Cu-R (Fig. 3f). Inductively coupled plasma-optical emission spectrometry (ICP-OES) analysis determined Pd and Pt loadings of approximately 4.2 wt% and 5.8 wt% in Pd-Cu₂O/Cu-R and Pt-Cu₂O/Cu-R, respectively. Transmission electron microscopy (TEM) analysis identified lattice spacings of 0.246 nm and 0.213 nm, corresponding to the Cu₂O (111) and (200) planes (Fig. 3g). Spacings of 0.213 nm for Cu₂O (200) and 0.224 nm for Pd (111) were resolved at the Pd/Cu₂O interface (Fig. 3i). Similarly, spacings of 0.213 nm for Cu₂O (200) and 0.195 nm for Pt (200) were measured at the Pt/Cu₂O interface in the Pt-Cu₂O/Cu-R composite (Fig. 3i).

Electrocatalytic properties of the NO₃RR

We systematically assessed nitrate reduction reaction performance in pretreated catalytic electrodes using a standard three-electrode H-cell configuration. Electrochemical evaluation in



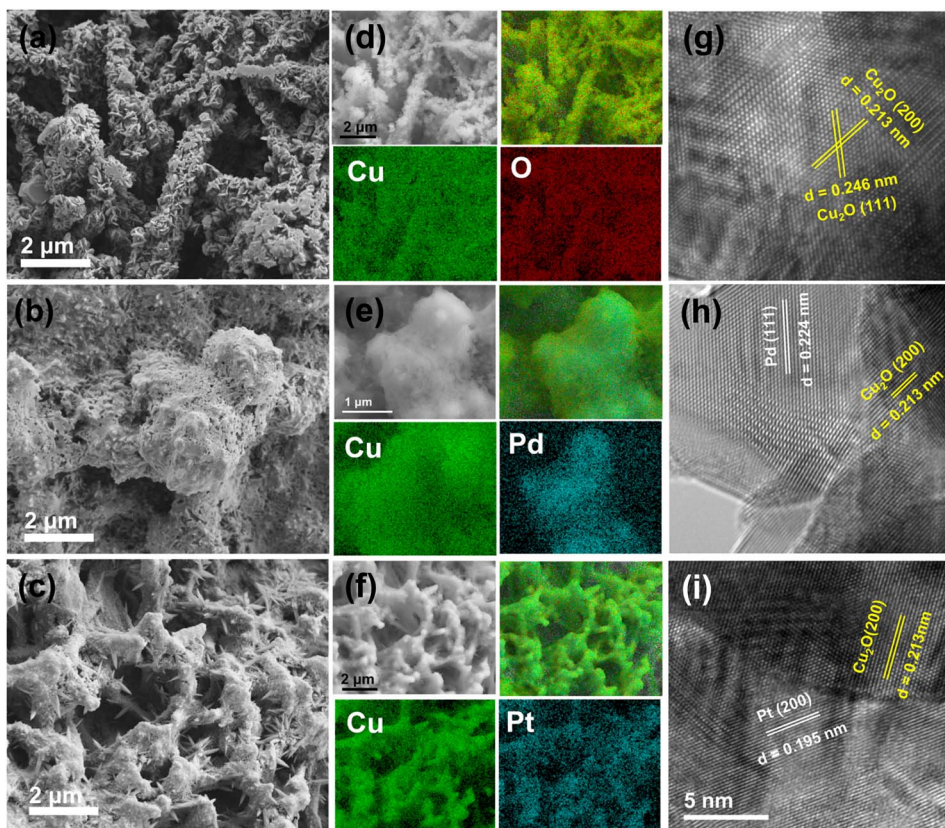


Fig. 3 SEM images of (a) $\text{Cu}_2\text{O}/\text{Cu-R}$; (b) $\text{Pd}-\text{Cu}_2\text{O}/\text{Cu-R}$ and (c) $\text{Pt}-\text{Cu}_2\text{O}/\text{Cu-R}$; the corresponding EDX mapping of (d) $\text{Cu}_2\text{O}/\text{Cu-R}$; (e) $\text{Pd}-\text{Cu}_2\text{O}/\text{Cu-R}$ and (f) $\text{Pt}-\text{Cu}_2\text{O}/\text{Cu-R}$; TEM images of (g) $\text{Cu}_2\text{O}/\text{Cu-R}$; (h) $\text{Pd}-\text{Cu}_2\text{O}/\text{Cu-R}$ and (i) $\text{Pt}-\text{Cu}_2\text{O}/\text{Cu-R}$.

0.1 M $\text{NaOH}/0.1 \text{ M } \text{NO}_3^-$ electrolyte revealed significant mass transport limitations from continuous nitrate depletion at the electrode interface, constraining electrocatalytic activity. To ensure efficient reactant supply, all experiments maintained constant 800 rpm agitation. Initial performance screening *via* chronoamperometry applied cathodic current densities from -25 to -125 mA cm^{-2} in identical electrolyte. Quantitative analysis of reduction products employed UV-visible absorption spectroscopy (Fig. S9–11), with comprehensive performance metrics, including $\text{NH}_3\text{-N}$ faradaic efficiency and yield rates, presented in Fig. 4a–c.

Electrocatalytic testing over a 2-hour period, with current–time profiles detailed in Fig. S12–14, revealed significant performance variations for the Cu_2O electrode during nitrate reduction. Notably, at 25 mA cm^{-2} , both the $\text{NH}_3\text{-N}$ yield rate and faradaic efficiency (FE) reached their minimum values of $0.31 \text{ mg h}^{-1} \text{ cm}^{-2}$ and 19.22% , respectively (Fig. 4a). The low FE strongly suggested insufficient generation of critical atomic hydrogen intermediates at this low current density. Performance improved at higher current densities, with the $\text{NH}_3\text{-N}$ yield rate peaking at $2.92 \text{ mg h}^{-1} \text{ cm}^{-2}$ at 100 mA cm^{-2} and $\text{NH}_3\text{-N}$ FE maximizing at 51.58% at 75 mA cm^{-2} . However, further increases in current density diminished both metrics, indicating that the hydrogen evolution reaction (HER) became increasingly dominant as a competing side reaction. Modification with precious metals markedly enhanced performance. Pd

loading elevated the $\text{NH}_3\text{-N}$ yield rate from $0.39 \text{ mg h}^{-1} \text{ cm}^{-2}$ at -25 mA cm^{-2} to $5.02 \text{ mg h}^{-1} \text{ cm}^{-2}$ at -125 mA cm^{-2} , while $\text{NH}_3\text{-N}$ FE rose from 23.92% at -25 mA cm^{-2} to a maximum of 75.39% at -75 mA cm^{-2} (Fig. 4b). Similarly, Pt loading boosted the yield rate from $0.82 \text{ mg h}^{-1} \text{ cm}^{-2}$ at -25 mA cm^{-2} to $5.14 \text{ mg h}^{-1} \text{ cm}^{-2}$ at -125 mA cm^{-2} and increased FE from 50.32% at -25 mA cm^{-2} to a peak of 86.55% at -75 mA cm^{-2} (Fig. 4c). Critically, for both $\text{Pd}-\text{Cu}_2\text{O}/\text{Cu-R}$ and $\text{Pt}-\text{Cu}_2\text{O}/\text{Cu-R}$, the $\text{NH}_3\text{-N}$ FE declined when the current density exceeded 75 mA cm^{-2} , a phenomenon again attributable to the heightened HER activity overwhelming the nitrate reduction pathway at excessive overpotentials. Under identical conditions, both precious-metal-modified electrodes consistently outperformed the bare Cu_2O , demonstrating that Pd and Pt loading synergistically enhanced electrocatalytic activity and selectivity for nitrate-to-ammonia conversion, with $\text{Pt}-\text{Cu}_2\text{O}/\text{Cu-R}$ exhibiting the highest overall performance.

In light of potential side reactions during the NO_3RR , the product selectivity efficiency (SE) of each catalytic electrode was systematically assessed. As shown in Fig. S15, the Cu_2O electrode exhibited predominant N_2 selectivity at current densities below 75 mA cm^{-2} , above which NO_2^- became the major product. With Pd modification, the electrode favoured NO_2^- formation, while Pt loading markedly enhanced NH_3 selectivity (Fig. S16 and S17). To enable a fair comparison of the intrinsic activity contributed by the noble metals, the NH_3 yield rate was



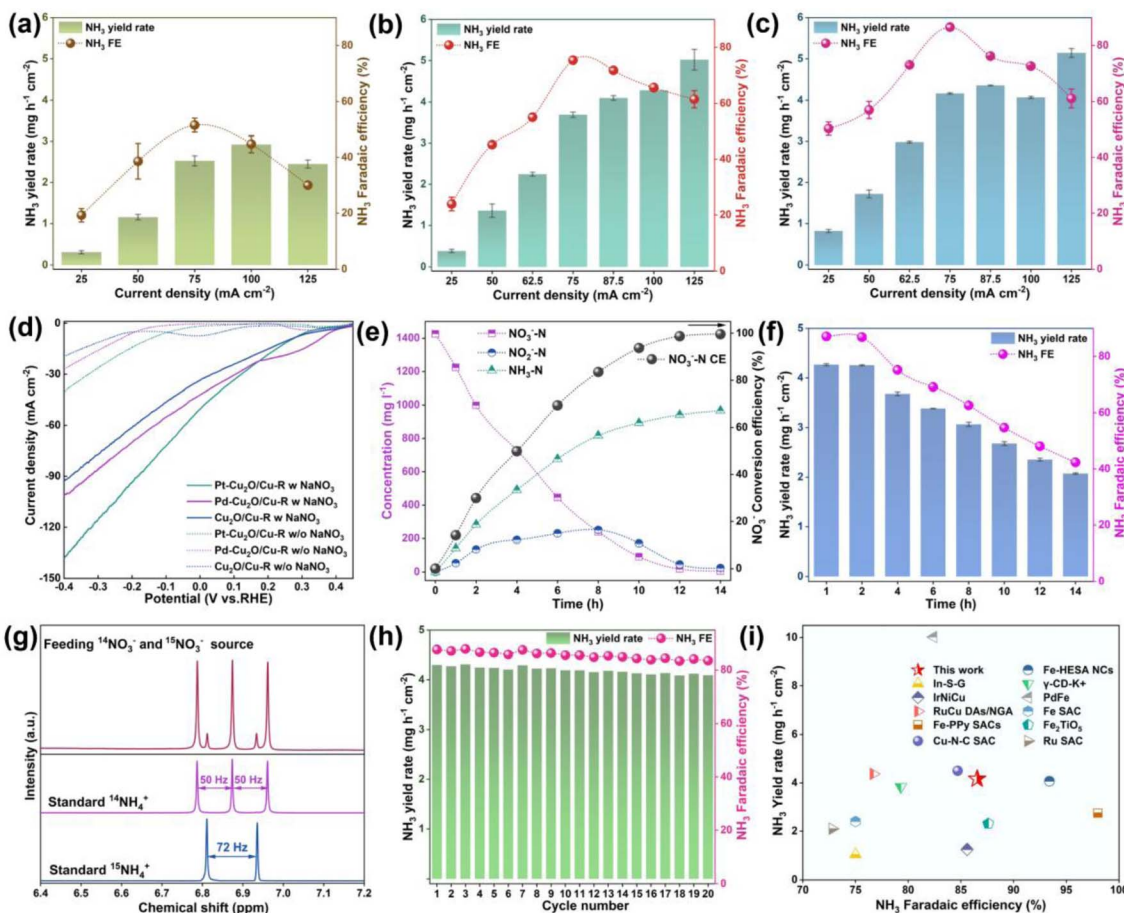


Fig. 4 Potentiostatic NO_3 RR: NH_3 -N yield rate and FE of (a) $\text{Cu}_2\text{O}/\text{Cu}-\text{R}$; (b) $\text{Pd}-\text{Cu}_2\text{O}/\text{Cu}-\text{R}$ and (c) $\text{Pt}-\text{Cu}_2\text{O}/\text{Cu}-\text{R}$; (d) LSV curves of $\text{Cu}_2\text{O}/\text{Cu}-\text{R}$, $\text{Pd}-\text{Cu}_2\text{O}/\text{Cu}-\text{R}$ and $\text{Pt}-\text{Cu}_2\text{O}/\text{Cu}-\text{R}$ without and with NO_3^- in 0.1 M NaOH ; Time-dependent variation of (e) NO_3^- -N, NO_2^- -N, and NH_3 -N concentration and NO_3 -N CE; (f) NH_3 -N yield rate and FE during the NO_3 RR; (g) ^1H NMR spectra of $\text{Pt}-\text{Cu}_2\text{O}/\text{Cu}-\text{R}$ after the NO_3 RR using $^{14}\text{NO}_3^-$ and $^{15}\text{NO}_3^-$; (h) stability test of the NO_3 RR for $\text{Pt}-\text{Cu}_2\text{O}/\text{Cu}-\text{R}$; (i) specific NH_3 -N yield rate of previously reported systems with different FEs for the NO_3 RR.

normalized by the mass of Pd or Pt, as quantified by ICP-OES. The resulting mass activity revealed that $\text{Pt}-\text{Cu}_2\text{O}/\text{Cu}-\text{R}$ consistently outperformed $\text{Pd}-\text{Cu}_2\text{O}/\text{Cu}-\text{R}$ across the tested current densities (Fig. S18).

Linear sweep voltammetry (LSV) tests performed on $\text{Cu}_2\text{O}/\text{Cu}-\text{R}$, $\text{Pd}-\text{Cu}_2\text{O}/\text{Cu}-\text{R}$, and $\text{Pt}-\text{Cu}_2\text{O}/\text{Cu}-\text{R}$ electrodes revealed significantly enhanced current densities for the $\text{Pd}-\text{Cu}_2\text{O}/\text{Cu}-\text{R}$ and $\text{Pt}-\text{Cu}_2\text{O}/\text{Cu}-\text{R}$ electrodes relative to Cu_2O in nitrate-free electrolyte, as depicted in Fig. 4d. Crucially, the presence of nitrate ions substantially increased the current density of all catalytic electrodes at identical applied potentials, directly indicating effective electrocatalytic nitrate reduction. The $\text{Pt}-\text{Cu}_2\text{O}/\text{Cu}-\text{R}$ electrode exhibited the most pronounced current density enhancement under these conditions, unequivocally demonstrating its superior intrinsic catalytic activity. Subsequent nitrate batch conversion test was conducted on the optimal $\text{Pt}-\text{Cu}_2\text{O}/\text{Cu}-\text{R}$ electrode in 0.1 M NaOH containing 0.1 M NO_3^- (1400 mg L^{-1}) at 75 mA cm^{-2} for 14 hours. Continuous nitrate degradation was observed, achieving near-complete removal by the 14-hour endpoint, while the intermediate nitrite was fully converted to the terminal products NH_3 -N

and N_2 , the latter partially escaping as gaseous N_2 (Fig. 4e). Notably, both the NH_3 -N yield rate and faradaic efficiency peaked at 2 hours before progressively declining over the remaining reaction time (Fig. 4f). This performance decay likely stemmed from the progressively depleted nitrate concentration diminishing the electrode's surface enrichment capacity, coupled with accumulating atomic hydrogen favouring the competing hydrogen evolution reaction. In addition, the $\text{Pd}-\text{Cu}_2\text{O}/\text{Cu}-\text{R}$ electrode was also tested under the same conditions for 14 h (Fig. S19). Finally, $^{14}\text{NO}_3^-/^{15}\text{NO}_3^-$ isotope labelling experiments analyzed by nuclear magnetic resonance unambiguously confirmed the nitrate source of the produced ammonia. Characteristic doublet peaks for $^{15}\text{NH}_4^+$ emerged when using $^{15}\text{NO}_3^-$ feedstock, while triplet peaks corresponding to $^{14}\text{NH}_4^+$ originated from $^{14}\text{NO}_3^-$, definitively verifying electrocatalytic nitrate reduction as the exclusive origin of ammonia, excluding contamination artifacts⁴¹ (Fig. 4g).

To evaluate the long-term operational stability of the Pt electrode, prolonged immersion was conducted within a solution containing 0.1 M NaOH and 0.1 M NO_3^- electrolytes, followed by 20 consecutive electrochemical cycle tests. As

evidenced in Fig. 4h, the Pt-Cu₂O/Cu-R electrode consistently achieved a stable NH₃-N faradaic efficiency of approximately 85.58% alongside an average NH₃-N yield rate of 4.19 mg h⁻¹ cm⁻² throughout these cycling experiments. To unequivocally verify the structural and chemical integrity of the Pt-Cu₂O/Cu-R electrode after extended operation, we employed a suite of post-test characterization techniques. *Ex situ* XPS analysis revealed that the chemical states remained largely unchanged: the Cu 2p spectrum was still dominated by Cu⁺/Cu⁰ signatures, with only a minor increase in Cu²⁺ satellites attributable to superficial air exposure, while the Pt 4f region maintained its mixed Pt⁴⁺/Pt⁰ character, indicating no significant agglomeration or leaching (Fig. S20). The negligible Pt and Cu dissolution was further corroborated by ICP-MS. Moreover, SEM imaging confirmed the preservation of the nanorod morphology without visible collapse or detachment (Fig. S21). This retained structural integrity directly accounted for the consistent electrochemical performance observed during cycling. This sustained high performance demonstrated robust preservation of active site integrity and confirmed the electrode's practical applicability under extended operational conditions. Furthermore, benchmarking against other catalytic systems confirms the superior performance of the Pt-Cu₂O/Cu-R electrode, positioning it among the most active catalysts reported to date (Fig. 4i and Table S1). While direct comparisons are constrained by differing experimental conditions across studies, the paramount advantage of our system lies in its well-balanced combination of high faradaic efficiency, remarkable NH₃ yield, and excellent operational durability, complemented by minimal metal leaching and a clearly elucidated synergistic mechanism. This holistic performance, supported by mechanistic insight and stability, establishes Pt-Cu₂O/Cu-R not only as a high-performing catalyst but also as a thoroughly understood and reliable material system, representing a meaningful step forward in nitrate reduction electrocatalysis.

Mechanisms of enhanced NO₃RR on Pt-Cu₂O/Cu-R

In situ electrochemical impedance spectroscopy (EIS) elucidated the interfacial charge transfer dynamics and provided indirect evidence for the enhanced reaction kinetics facilitated by the precious metals (Fig. S22). Analysis of Bode phase plots (Fig. 5a-c) across applied potentials revealed a systematic decrease in phase angle peak magnitude concurrent with a shift towards higher frequencies upon cathodic polarization.⁴² This behaviour is characteristic of a diminishing faradaic resistance and an acceleration of the rate-determining step(s) of the surface reaction. The critical insight comes from comparing the EIS response in different electrolytes. This modulation of the phase angle (decrease and frequency shift) progressed more rapidly and was more pronounced in nitrate-containing electrolytes compared to nitrate-free conditions. This demonstrates that the presence of nitrate actively lowers the activation barrier for the charge transfer process, consistent with the initiation of the NO₃RR.

Furthermore, the Pd-Cu₂O/Cu-R and Pt-Cu₂O/Cu-R electrodes exhibited a more substantial displacement of the phase

angle peak towards higher frequencies relative to the unmodified Cu₂O/Cu-R electrode under identical conditions. In the context of the NO₃RR, which involves multiple proton-coupled electron transfers, the rate of the overall process is often limited by the supply of reactive hydrogen intermediates (H). A significant reduction in charge transfer resistance, as indicated by the EIS data, strongly suggested that the incorporated noble metal sites are facilitating a key step that provides these species. We posited that this step was the dissociation of water (H₂O + e⁻ → H + OH⁻), which is the primary proton source in alkaline media. The more efficient this dissociation, the faster the subsequent formation of H and the hydrogenation of N-intermediates can occur, leading to the observed lower impedance. The Pt-Cu₂O/Cu-R electrode displayed the most pronounced effect, exhibiting significantly reduced phase angles compared to Pd-Cu₂O/Cu-R. This difference directly correlates with platinum's superior capability, as an oxidized species (Pt⁴⁺), to activate water molecules and stabilize the resulting *H intermediates, a conclusion subsequently supported by our CV and EPR results, which showed greater H generation and consumption on Pt. Therefore, the EIS trends provide strong, correlative evidence that the precious metals, particularly Pt, enhance the kinetics of the NO₃RR by optimizing the interfacial environment for water dissociation and hydrogen intermediate stabilization.

The critical role of reactive atomic hydrogen intermediates in nitrate deoxygenation and hydrogenation is well-established. To directly monitor these H* species, we performed *in situ* CV with varied starting potentials. As shown in Fig. 5d, voltammograms for pristine Cu₂O and Pd/Pt-Cu₂O/Cu-R in nitrate-free electrolyte exhibited two distinct oxidation peaks during the positive scan, attributable to hydrogen gas oxidation and adsorbed hydrogen species oxidation, respectively⁴³ (Fig. 5d and S17). Notably, the significantly higher peak intensities observed on the Pt-Cu₂O/Cu-R electrode directly implicate Pt sites as primary centres for efficient H* activation (Fig. S23). Crucially, the introduction of nitrate into the electrolyte caused the complete disappearance of these H-associated oxidation peaks, providing direct electrochemical evidence for H consumption during nitrate reduction. This participation of atomic hydrogen was further corroborated by electron paramagnetic resonance spectroscopy probing DMPO-H adduct formation. Fig. 5e reveals the characteristic nine-line EPR signature of DMPO-H for the Cu oxide-based catalyst in 0.1 M NaOH, with signal intensity progressively strengthening over reaction time.⁴⁴ Mirroring the CV observations, the addition of nitrate to the NaOH solution resulted in clear attenuation and ultimate disappearance of these nine-line peaks, as shown in Fig. 5f, unequivocally confirming the involvement of atomic hydrogen intermediates in driving nitrate reduction.

To probe the superior nitrate reduction reaction (NO₃RR) catalytic activity of Pt-Cu₂O/Cu-R, we conducted *in situ* Raman spectroscopy under operational conditions. Comparative spectra for Cu₂O/Cu-R were also acquired across a potential range in 0.1 M NaOH containing 0.1 M NO₃⁻. Initial characterization at open circuit potential (OCP) revealed the definitive presence of Cu₂O within both Pt-Cu₂O/Cu-R and Cu₂O/Cu-R,



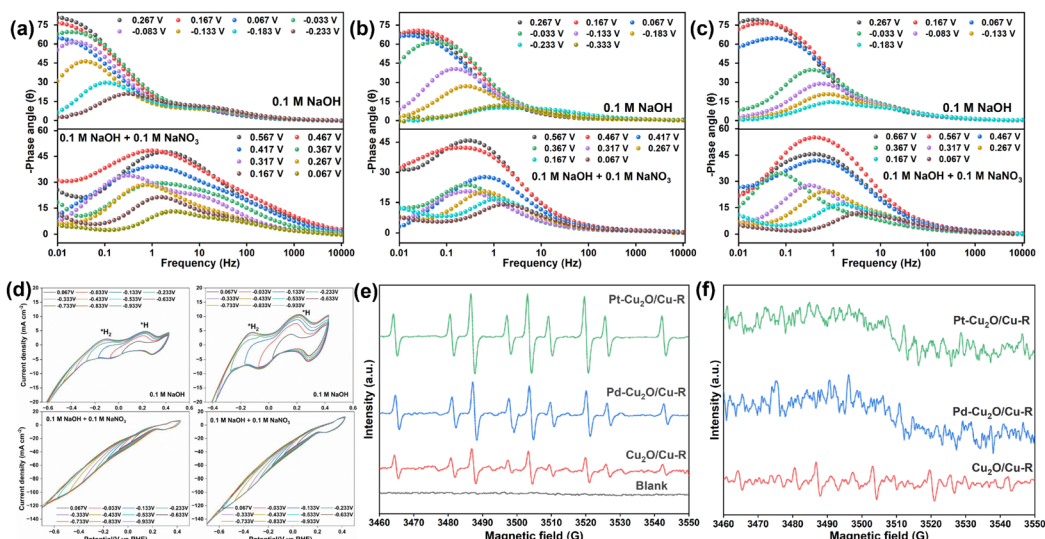


Fig. 5 Bode phase plots of (a) $\text{Cu}_2\text{O}/\text{Cu-R}$; (b) $\text{Pd}-\text{Cu}_2\text{O}/\text{Cu-R}$ and (c) $\text{Pt}-\text{Cu}_2\text{O}/\text{Cu-R}$ in different electrolytes under various electrochemical conditions; (d) CV curves of (left) $\text{Cu}_2\text{O}/\text{Cu-R}$ and (right) $\text{Pd}-\text{Cu}_2\text{O}/\text{Cu-R}$ in 0.1 M NaOH , with or without addition of $0.1 \text{ M } \text{NO}_3^-$; (e) EPR spectra of $\text{Cu}_2\text{O}/\text{Cu-R}$, $\text{Pd}-\text{Cu}_2\text{O}/\text{Cu-R}$ and $\text{Pt}-\text{Cu}_2\text{O}/\text{Cu-R}$ in 0.1 M NaOH ; (f) EPR spectra with added NO_3^- .

signified by characteristic vibrational peaks at 148, 218, and 625 cm^{-1} .⁴⁵ A critical observation emerged as the applied potential was swept negatively. These Cu_2O signatures progressively diminished in intensity within the $\text{Cu}_2\text{O}/\text{Cu-R}$ sample, ultimately vanishing completely at 0 V *versus* RHE. This behaviour directly indicated the electrochemical reduction of

Cu^+ species to metallic copper (Cu^0) during the NO_3RR (Fig. 6a). Strikingly, the $\text{Pt}-\text{Cu}_2\text{O}/\text{Cu-R}$ catalyst exhibited markedly different behavior; although attenuated, the characteristic Cu_2O Raman signals, particularly those at 148, 218, and 625 cm^{-1} , persisted discernibly throughout the entire applied potential window. This sustained presence provided compelling

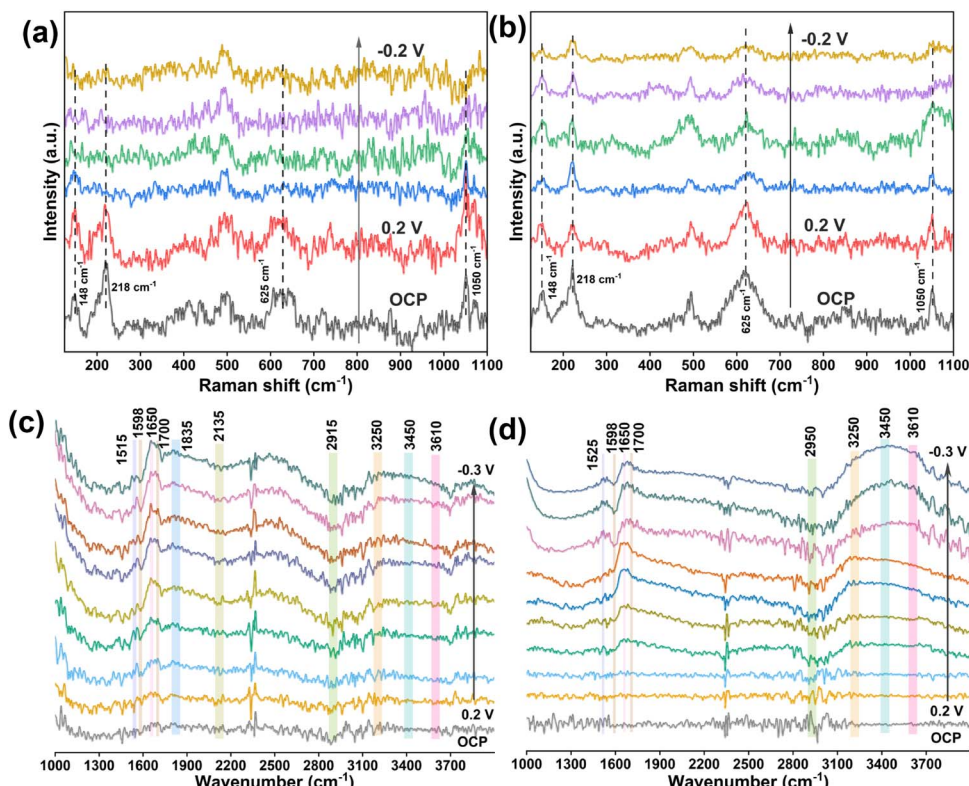


Fig. 6 *In situ* Raman spectra of (a) $\text{Cu}_2\text{O}/\text{Cu-R}$ and (b) $\text{Pt}-\text{Cu}_2\text{O}/\text{Cu-R}$ for the NO_3RR at different potentials; *in situ* FTIR spectra of (c) $\text{Cu}_2\text{O}/\text{Cu-R}$ and (d) $\text{Pt}-\text{Cu}_2\text{O}/\text{Cu-R}$ for the NO_3RR at different potentials.

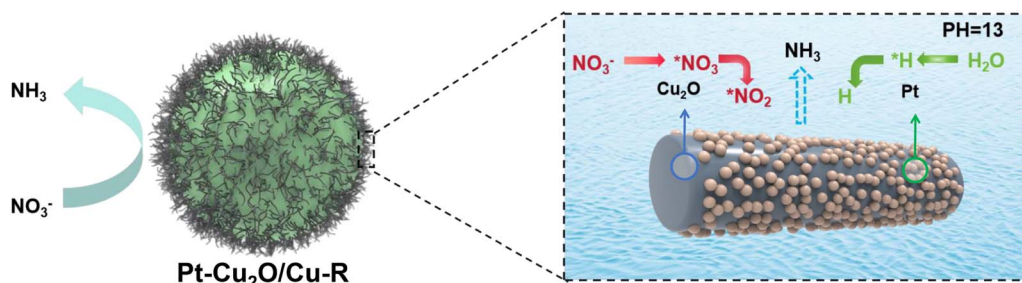


Fig. 7 Schematic representation of the NO_3 RR active sites on the surface of the Pt– $\text{Cu}_2\text{O}/\text{Cu-R}$ electrode at pH 13. This schematic integrates the key experimental findings of this work: the stabilization of Cu^+ sites, the critical role of atomic $^*\text{H}$ supplied from Pt-facilitated water dissociation, and the detection of key nitrogenous intermediates.

spectroscopic evidence that the incorporation of Pt^{4+} ions significantly enhances the structural stability of the Cu_2O phase, specifically stabilizing the $\text{Cu}^+–\text{O}$ bonding framework against cathodic reduction under reaction conditions. Concurrently, the Raman signature of nitrate ions, identified by its characteristic peak centered near 1050 cm^{-1} , was monitored, offering insight into the interfacial reaction environment (Fig. 6b).⁴⁶

The striking contrast in the stability of Cu^+ species between Pt– $\text{Cu}_2\text{O}/\text{Cu-R}$ and the unmodified catalyst, as revealed by *in situ* Raman, pointed to a strong metal–support interaction (SMSI) that electronically stabilized the Cu_2O matrix. We proposed that this stabilization originated from electron transfer at the Pt– Cu_2O interface. Our XPS analysis (Fig. 2f) showed that Pt species are predominantly present in an oxidized state (Pt^{4+}), suggesting partial charge transfer from the Cu_2O support to Pt. This electronic redistribution contributes to Cu^+ stabilization in two key ways: (i) it rendered the Cu centres in Cu_2O slightly electron-deficient, which raises the energy barrier for their reduction to Cu^0 by hindering further electron uptake from the cathode; (ii) it strengthened the Pt–O–Cu linkage at the interface, thereby enhancing the structural integrity of the Cu_2O phase and improving its resistance to cathodic decomposition.

Complementary *in situ* FTIR spectroscopy tracked evolving interfacial species during the NO_3 RR across potentials from open circuit to -0.3 V , as detailed in Fig. 6c and d. Spectra for the $\text{Cu}_2\text{O}/\text{Cu-R}$ electrode revealed the sequential emergence and intensification of key intermediate signatures: a peak near 1515 cm^{-1} assigned to H–N–H bending, $^*\text{N–O}$ stretching near 1600 cm^{-1} , adsorbed $^*\text{NO}_3$ species at 1700 cm^{-1} , $^*\text{NO}$ species near 1835 cm^{-1} , and $^*\text{N–H}$ stretching vibration near 2950 cm^{-1} indicative of $^*\text{NH}_3$ formation.^{47–50} This progression confirms the electrocatalytic deoxygenation and hydrogenation pathway generating ammonia. Concurrently, a downward feature at 2136 cm^{-1} signifying $\text{N}=\text{N}$ stretching provided evidence for dinitrogen formation as a minor pathway.⁵¹ Further spectral regions exhibited upward bands: the H–O–H bending mode near 1650 cm^{-1} and a broad O–H stretching envelope between 3000 and 3700 cm^{-1} encompassing contributions from ice-like water near 3250 cm^{-1} , liquid-like water near 3450 cm^{-1} , and free water near 3610 cm^{-1} .⁵² Crucially, comparative analysis demonstrated a pronounced enhancement in the liquid-like

and free water bands for the Pt– $\text{Cu}_2\text{O}/\text{Cu-R}$ electrode relative to pristine $\text{Cu}_2\text{O}/\text{Cu-R}$, particularly at low applied potentials. This distinct spectral evolution directly indicated significantly more effective water dissociation occurring at the Pt– Cu_2O interface, where the electrophilic Pt^{4+} species facilitate the initial interaction with water molecules, thereby enhancing the local proton supply critical for the hydrogenation steps of nitrate reduction. This finding provides direct spectroscopic support for the enhanced interfacial kinetics inferred from the EIS analysis (Fig. 5c), confirming that Pt sites efficiently facilitate the proton-supplying step critical for the hydrogenation steps of nitrate reduction.

Based on the collective *in situ* spectroscopic and electrochemical evidence, we propose the synergistic reaction mechanism for the significantly enhanced nitrate-to-ammonia reduction activity. Platinum sites efficiently dissociate water molecules, providing a critical source of reactive hydrogen intermediates. Concurrently, *in situ* generated Cu_2O was identified as the primary active plane for nitrate reduction catalysis, as illustrated in Fig. 7. While the exact adsorption geometries of the intermediates are simplified representations, the identified species and the overall bifunctional pathway are directly corroborated by our experimental data. The sequential hydrogenation process from $^*\text{NO}_3$ to NH_3 , involving the detected intermediates (NO_2 , $^*\text{NO}$, and $^*\text{NH}_2$), aligns with widely accepted mechanisms for nitrate electroreduction on copper-based catalysts.^{4,40} Crucially, this bifunctional architecture optimally balances competing reaction kinetics: it promotes the nitrate reduction pathway leading to ammonia synthesis while simultaneously moderating the consumption of atomic hydrogen intermediates through parasitic hydrogen evolution. This strategic kinetic regulation directly underpins the catalyst's exceptional activity, enabling high-efficiency ammonia production at substantially reduced overpotentials.

Conclusion

This study systematically evaluates the electrocatalytic nitrate reduction performance of Pt– $\text{Cu}_2\text{O}/\text{Cu-R}$ and Pd– $\text{Cu}_2\text{O}/\text{Cu-R}$ electrodes. The Pt– $\text{Cu}_2\text{O}/\text{Cu-R}$ electrode demonstrates superior activity, achieving a maximum ammonia-N faradaic efficiency of 86.55% and a yield rate of $4.16\text{ mg h}^{-1}\text{ cm}^{-2}$, significantly



exceeding the performance of both Pd-Cu₂O/Cu-R and unmodified Cu₂O/Cu-R. *In situ* Raman spectroscopy confirmed the critical persistence of stable Cu⁺ species throughout nitrate reduction. These Cu⁺ sites actively activate nitrogen-containing intermediates, while neighbouring platinum sites facilitate water dissociation to supply essential hydrogen species for intermediate hydrogenation. Complementary *in situ* FTIR spectroscopy revealed that the Pt-Cu₂O/Cu-R architecture promotes efficient accumulation and conversion of nitrite intermediates while optimizing the configuration of key *NO intermediates to favour subsequent hydrogenation steps. Cyclic voltammetry and electron spin resonance spectroscopy definitively identified the reactive H species central to this mechanism. These findings establish a vital strategy for stabilizing active Cu⁺ catalytic centres *via* the creation of electron-deficient Cu sites through charge transfer to oxidized Pt species, and elucidate fundamental mechanistic insight into synergistic nitrate reduction pathways, paving the way for the design of advanced catalysts based on electronic-structure modulation.

Author contributions

Wenzheng Yu and Kai Zhang designed the experiments; Xiaolong Zhu and Kai Zhang completed the main experiments and wrote the draft; Jiahao Tao and Siyi Liang were involved in some experiments; Rong Chen and Wenzheng Yu made the final revision to the manuscript.

Conflicts of interest

There are no conflicts to declare.

Data availability

The data supporting this article have been included as part of the supplementary information (SI). Supplementary information: additional supporting figures, tables, and experimental procedures are provided in the SI. See DOI: <https://doi.org/10.1039/d5ta06839h>.

Acknowledgements

This research was financially supported by the Key Research and Development Plan of the Ministry of Science and Technology (2023YFC3207903), National Natural Science Foundation of China (Grants 52000178 and 52370184) and special fund of State Key Laboratory of Regional Environment and Sustainability (25K10REST). The authors would like to thank Shiyanjia Lab (<https://www.shyanjia.com>) for the SEM and XPS analysis.

References

- 1 P. H. van Langevelde, I. Katsounaros and M. T. Koper, *Joule*, 2021, **5**, 290–294.
- 2 S. Garcia-Segura, M. Lanzarini-Lopes, K. Hristovski and P. Westerhoff, *App. Catal. B: Environ.*, 2018, **236**, 546–568.
- 3 M. H. Ward, R. R. Jones, J. D. Brender, T. M. De Kok, P. J. Weyer, B. T. Nolan, C. M. Villanueva and S. G. Van Breda, *Int. J. Environ. Res. Public Health*, 2018, **15**, 1557.
- 4 G. Zhang, B. Li, Y. Shi, Q. Zhou, W.-J. Fu, G. Zhou, J. Ma, S. Yin, W. Yuan, S. Miao, Q. Ji, J. Qu and H. Liu, *Nat. Sustain.*, 2024, **7**, 1251–1263.
- 5 M. Duca and M. T. Koper, *Energy Environ. Sci.*, 2012, **5**, 9726–9742.
- 6 S. Zhang, J. Wu, M. Zheng, X. Jin, Z. Shen, Z. Li, Y. Wang, Q. Wang, X. Wang and H. Wei, *Nat. Commun.*, 2023, **14**, 3634.
- 7 N. Barrabés and J. Sá, *App. Catal. B: Environ.*, 2011, **104**, 1–5.
- 8 Z. Ni, C. Luo, B. Cheng, P. Kuang, Y. Li and J. Yu, *App. Catal. B: Environ.*, 2023, **321**, 122072.
- 9 Y. Hua, N. Song, Z. Wu, Y. Lan, H. Luo, Q. Song and J. Yang, *Adv. Funct. Mater.*, 2024, **34**, 2314461.
- 10 Z.-Y. Wu, M. Karamad, X. Yong, Q. Huang, D. A. Cullen, P. Zhu, C. Xia, Q. Xiao, M. Shakouri and F.-Y. Chen, *Nat. Commun.*, 2021, **12**, 2870.
- 11 Y.-J. Shih, Z.-L. Wu and Y.-C. He, *J. Hazard. Mater.*, 2024, **477**, 135276.
- 12 P. Wang, S. Meng, B. Zhang, M. He, P. Li, C. Yang, G. Li and Z. Li, *J. Am. Chem. Soc.*, 2023, **145**, 26133–26143.
- 13 K. Huang, K. Tang, M. Wang, Y. Wang, T. Jiang and M. Wu, *Adv. Funct. Mater.*, 2024, **34**, 2315324.
- 14 B. Zhang, Z. Dai, Y. Chen, M. Cheng, H. Zhang, P. Feng, B. Ke, Y. Zhang and G. Zhang, *Nat. Commun.*, 2024, **15**, 2816.
- 15 Y. Liu, C. Kong, L. Liu, X. Jiang, C. Liu, F. Liu, J. Sun and Y. Wang, *Chem. Eng. J.*, 2024, 150217.
- 16 X. Zhu, K. Dong, D. T. Tran, S. Sidra, D. C. Nguyen, D. H. Kim, N. H. Kim and J. H. Lee, *Small*, 2025, **21**, 2405452.
- 17 M. D. Marcinkowski, M. T. Darby, J. Liu, J. M. Wimble, F. R. Lucci, S. Lee, A. Michaelides, M. Flytzani-Stephanopoulos, M. Stamatakis and E. C. H. Sykes, *Nat. Chem.*, 2018, **10**, 325–332.
- 18 Z. Xiong, Z. Lei, C.-C. Kuang, X. Chen, B. Gong, Y. Zhao, J. Zhang, C. Zheng and J. C. Wu, *App. Catal. B: Environ.*, 2017, **202**, 695–703.
- 19 J. Su, K. Shi, B. Liu, Z. Xi, J. Yu, X. Xu, P. Jing, R. Gao and J. Zhang, *Adv. Funct. Mater.*, 2024, **34**, 2401194.
- 20 H. Liu, X. Lang, C. Zhu, J. Timoshenko, M. Rüscher, L. Bai, N. Guijarro, H. Yin, Y. Peng and J. Li, *Angew. Chem., Int. Ed.*, 2022, **61**, e202202556.
- 21 R. Liu, H. Zhao, X. Zhao, Z. He, Y. Lai, W. Shan, D. Bekana, G. Li and J. Liu, *Environ. Sci. Technol.*, 2018, **52**, 9992–10002.
- 22 A. Tayal, O. Seo, J. Kim, H. Kobayashi, T. Yamamoto, S. Matsumura, H. Kitagawa and O. Sakata, *ACS Appl. Mater. Interfaces*, 2021, **13**, 23502–23512.
- 23 C. A. Boasiako, Z. Zhou, X. Huo and T. Ye, *J. Hazard. Mater.*, 2023, **446**, 130661.
- 24 O. Soares, J. Órfão, J. Ruiz-Martínez, J. Silvestre-Albero, A. Sepúlveda-Escribano and M. Pereira, *Chem. Eng. J.*, 2010, **165**, 78–88.
- 25 H. Zhu, J. J. Wang, Z. Xu, Y. Tan and J. Wang, *Small*, 2024, **20**, 2404919.
- 26 H. Guo, M. Li, Y. Yang, R. Luo, W. Liu, F. Zhang, C. Tang, G. Yang and Y. Zhou, *Small*, 2023, **19**, 2207743.



27 G. A. Cerrón-Calle, A. S. Fajardo, C. M. Sánchez-Sánchez and S. García-Segura, *App. Catal. B: Environ.*, 2022, **302**, 120844.

28 T. Chen, H. Li, H. Ma and M. T. Koper, *Langmuir*, 2015, **31**, 3277–3281.

29 K. Zhang, B. Li, F. Guo, N. Graham, W. He and W. Yu, *Angew. Chem., Int. Ed.*, 2024, **136**, e202411796.

30 Y. Wang, W. Zhou, R. Jia, Y. Yu and B. Zhang, *Angew. Chem., Int. Ed.*, 2020, **59**, 5350–5354.

31 H. Choi, M. Jun, W. Kang, T. Kim, S. Choi, C. Choi, H. Wang, H. Baik, Y. Jung and K. Jin, *Chem Catal.*, 2024, **4**, 101029.

32 M. Hasnat, S. B. Aoun, S. N. Uddin, M. M. Alam, P. Koay, S. Amertharaj, M. Rashed, M. M. Rahman and N. Mohamed, *Appl. Catal., A*, 2014, **478**, 259–266.

33 A. Aristizábal, S. Contreras, N. Barrabés, J. Llorca, D. Tichit and F. Medina, *App. Catal. B: Environ.*, 2011, **110**, 58–70.

34 L. Xiao, W. Dai, S. Mou, X. Wang, Q. Cheng and F. Dong, *Energy Environ. Sci.*, 2023, **16**, 2696–2704.

35 T. Ma, H. Cao, S. Li, S. Cao, Z. Zhao, Z. Wu, R. Yan, C. Yang, Y. Wang and P. A. van Aken, *Adv. Mater.*, 2022, **34**, 2206368.

36 P. P. Yang, X. L. Zhang, F. Y. Gao, Y. R. Zheng, Z. Z. Niu, X. Yu, R. Liu, Z. Z. Wu, S. Qin, L. P. Chi, Y. Duan, T. Ma, X. S. Zheng, J. F. Zhu, H. J. Wang, M. R. Gao and S. H. Yu, *J. Am. Chem. Soc.*, 2020, **142**, 6400–6408.

37 Y. Cheng, Q. Li, M. I. B. Salaman, C. Wei, Q. Wang, X. Ma, B. Liu and A. B. Wong, *J. Am. Chem. Soc.*, 2025, **147**, 12438–12448.

38 C. Liu, M. Wang, J. Ye, L. Liu, L. Li, Y. Li and X. Huang, *Nano Lett.*, 2023, **23**, 1474–1480.

39 M. Jiang, J. Xu, Q. Zhou, Y. Chen, P. Munroe, L. Li, Z.-H. Xie, Y. Wu and S. Peng, *Angew. Chem., Int. Ed.*, 2025, e202510259.

40 F. Dou, F. Guo, B. Li, K. Zhang, N. Graham and W. Yu, *J. Hazard. Mater.*, 2024, **472**, 134522.

41 K. Zhang, B. Li, F. Guo, N. Graham, W. He and W. Yu, *Angew. Chem., Int. Ed.*, 2024, **63**, e202411796.

42 H. Xu, G. Xu, B. Huang, J. Yan, M. Wang, L. Chen and J. Shi, *Angew. Chem., Int. Ed.*, 2023, **62**, e202218603.

43 W. Zheng, L. Zhu, Z. Yan, Z. Lin, Z. Lei, Y. Zhang, H. Xu, Z. Dang, C. Wei and C. Feng, *Environ. Sci. Technol.*, 2021, **55**, 13231–13243.

44 K. Fan, W. Xie, J. Li, Y. Sun, P. Xu, Y. Tang, Z. Li and M. Shao, *Nat. Commun.*, 2022, **13**, 7958.

45 Y. Deng, A. D. Handoko, Y. Du, S. Xi and B. S. Yeo, *ACS Catal.*, 2016, **6**, 2473–2481.

46 W. He, J. Zhang, S. Dieckhofer, S. Varhade, A. C. Brix, A. Lielpetere, S. Seisel, J. R. C. Junqueira and W. Schuhmann, *Nat. Commun.*, 2022, **13**, 1129.

47 K. Chen, Y. Zhang, J. Xiang, X. Zhao, X. Li and K. Chu, *ACS Energy Lett.*, 2023, **8**, 1281–1288.

48 Z.-H. Xue, H.-C. Shen, P. Chen, G.-X. Pan, W.-W. Zhang, W.-M. Zhang, S.-N. Zhang, X.-H. Li and C. T. Yavuz, *ACS Energy Lett.*, 2023, **8**, 3843–3851.

49 Z. Gong, W. Zhong, Z. He, Q. Liu, H. Chen, D. Zhou, N. Zhang, X. Kang and Y. Chen, *App. Catal. B: Environ.*, 2022, **305**, 121021.

50 N. C. Kani, J. A. Gauthier, A. Prajapati, J. Edgington, I. Bordawekar, W. Shields, M. Shields, L. C. Seitz, A. R. Singh and M. R. Singh, *Energy Environ. Sci.*, 2021, **14**, 6349–6359.

51 H. Hirakawa, M. Hashimoto, Y. Shiraishi and T. Hirai, *J. Am. Chem. Soc.*, 2017, **139**, 10929–10936.

52 K. Sun, X. Wu, Z. Zhuang, L. Liu, J. Fang, L. Zeng, J. Ma, S. Liu, J. Li, R. Dai, X. Tan, K. Yu, D. Liu, W. C. Cheong, A. Huang, Y. Liu, Y. Pan, H. Xiao and C. Chen, *Nat. Commun.*, 2022, **13**, 6260.

